

# Visual Exploration of Nasal Airflow

Stefan Zachow, *Member, IEEE*, Philipp Muigg, Thomas Hildebrandt, Helmut Doleisch, *Member, IEEE*, and Hans-Christian Hege, *Member, IEEE*

**Abstract**—Rhinologists are often faced with the challenge of assessing nasal breathing from a functional point of view to derive effective therapeutic interventions. While the complex nasal anatomy can be revealed by visual inspection and medical imaging, only vague information is available regarding the nasal airflow itself: Rhinomanometry delivers rather unspecific integral information on the pressure gradient as well as on total flow and nasal flow resistance. In this article we demonstrate how the understanding of physiological nasal breathing can be improved by simulating and visually analyzing nasal airflow, based on an anatomically correct model of the upper human respiratory tract. In particular we demonstrate how various Information Visualization (InfoVis) techniques, such as a highly scalable implementation of parallel coordinates, time series visualizations, as well as unstructured grid multi-volume rendering, all integrated within a multiple linked views framework, can be utilized to gain a deeper understanding of nasal breathing. Evaluation is accomplished by visual exploration of spatio-temporal airflow characteristics that include not only information on flow features but also on accompanying quantities such as temperature and humidity. To our knowledge, this is the first in-depth visual exploration of the physiological function of the nose over several simulated breathing cycles under consideration of a complete model of the nasal airways, realistic boundary conditions, and all physically relevant time-varying quantities.

**Index Terms**—Flow visualization, exploratory data analysis, interactive visual analysis of scientific data, time-dependent data.

## 1 INTRODUCTION

In otorhinolaryngology (a medical specialty concerned with diseases of the Ear, Nose, and Throat), ENT specialists are often confronted with the challenge of assessing nasal breathing from a functional point of view. Due to the anatomical situation, direct measurements within the nose are not possible without influencing the airflow itself. Besides a visual inspection of the nasal airways with regard to obstruction and deformities, as well as medical imaging as a diagnostic means, the only objective measurement of nasal airflow is rhinomanometry which, however, delivers rather unspecific integral information on the pressure gradient as well as on total flow or flow resistance. Thus, physiological function of the nose cannot be assessed sufficiently and therapeutic concepts are difficult to derive.

In cases of pathological nasal breathing a surgical correction might be indicated. Rhinosurgery is a reconstructive surgical approach that reshapes the external nose and/or inner structures of the nasal cavities with the objective of re-establishing *normal nasal breathing*. Though treatment methods in ENT surgery have constantly improved, the appraisal of a promising individual therapy under consideration of *regular nasal airflow* is still a challenging task. Very often too radical resection of turbinate mucosal tissue results in a so-called empty nose syndrome (ENS). There is, however, no standard of how much turbinate tissue has to be removed to re-establish physiological breathing. Nor is it known how much tissue can be removed before it causes other damage to the physiology of the nose. An in-depth knowledge of normal nose breathing, as well as an understanding of the relationship between morphology and physiology of the nose will be the foundation for an improved rehabilitation in functional rhinosurgery.

Our objective is to analyze and to understand the physiology and pathophysiology of nasal breathing. To this end, airflow simulations based on computational fluid dynamics (CFD) have been conducted

for a highly detailed anatomy of the upper respiratory tract from the external nose deep into the trachea, including frontal and maxillary sinuses, as well as the ethmoid [41, 40]. Besides the creation of a highly detailed model of the upper respiratory tract from CT data (cf. Figs. 1 and 3), the major contribution of this work is the visual exploration of transient airflow simulation results in order to detect and distinguish characteristic airflow patterns within nasal breathing cycles.

In particular we demonstrate how highly scalable techniques for Information Visualization (InfoVis) such as parallel coordinates, time series visualizations, and unstructured grid multi-volume rendering, all integrated within a multiple linked views framework, can be utilized to gain a deeper understanding of nasal breathing. Evaluation is accomplished by visual exploration of spatio-temporal airflow characteristics that include not only information regarding flow features but also on accompanying quantities such as temperature and humidity.

Our long-term goal is to gain insight into the relationship between morphology of nasal airways and flow behavior in order to 1) better understand physiological nose breathing, 2) distinguish between regular and irregular airflow, and to 3) develop planning tools for decision support in functional rhinosurgery.

### 1.1 Related Work

The function of the human nose is diverse, ranging from breathing and smelling to humidification, warming, and cleaning of the inhaled air. For patients with a functional impairment of the nose, however, it is neither clear how to assess the individual function of the nose, nor how to re-establish regular nose breathing. In fact, it is even unclear what *regular* nose breathing is. Thus, there is a great demand for understanding the physiology and pathophysiology of nasal breathing in functional rhinosurgery [25]. With constantly increasing computational performance as well as advances in modeling and simulation of complex problems in applied mathematics and engineering, CFD has become an attractive means for predicting fluid flow in a variety of bioengineering problems [21]. In medical applications, for example, CFD methods have been successfully applied for blood flow simulations [12]. Several research groups have also demonstrated that CFD is basically applicable to analyze airflow phenomena in the nose. Investigations vary from general analysis of nasal airflow including experimental work [18, 2, 10], to simulations with respect to morphology changes [11], odorant transport [43], temperature distribution [29, 24], and aerosol distribution [32], up to a decision support for rhinosurgery [23, 13, 39].

- Stefan Zachow and Hans-Christian Hege are with Zuse Institute Berlin (ZIB), Germany, E-mail: {zachow, hege}@zib.de .
- Thomas Hildebrandt is with the Asklepios Clinic Birkenwerder, Section Rhinosurgery, Germany, E-mail: th@rhinosurgery.de .
- Philipp Muigg is with the Institute of Computer Graphics and Algorithms, Vienna University of Technology. Both Philipp and Helmut Doleisch are with SimVis GmbH, Austria, E-mail: {muigg, doleisch}@simvis.at .

Manuscript received 31 March 2009; accepted 27 July 2009; posted online 11 October 2009; mailed on 5 October 2009.

For information on obtaining reprints of this article, please send email to: tvcg@computer.org .

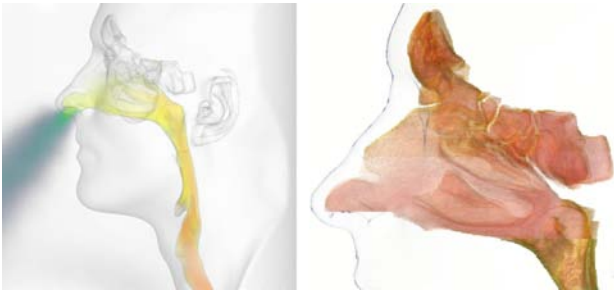


Fig. 1. Model of the upper respiratory tract (left), nasal cavities (right).

The visualization of CFD simulation results (flow visualization), is a broad area of research mainly dealing with 2-D, 3-D or even 4-D vector fields. Good surveys of commonly used methods are given, for example, by Post et al. and Laramee et al. [30, 22]. Especially when dealing with more complex simulation models that incorporate not only flow but also data about processes (such as combustion, chemical reactions, or meteorological phenomena), interactive exploration and analysis techniques have gained importance. Gresh et al. [15] were among the first using interactive visual analysis methods such as multiple linked views (attribute space as well as 3-D visualizations) for the analysis of scientific simulation data. Doleisch et al. extended previous binary brushing approaches by proposing smooth brushing [7], and introducing more complex feature definition concepts in combination with focus+context visualization [6, 5]. Meanwhile, interactive visual analysis frameworks are well-established in many other application areas such as automotive engineering [8], meteorology [9], and climate research [20].

Since most CFD simulation data are either of spatial (3-D) or spatio-temporal (4-D) nature and typically large in size, it is important for the visual exploration process to provide highly responsive volume visualization techniques. In order to retain interactivity, a GPU implementation of an unstructured grid ray-casting method [14], comparable to the implementation of Weiler et al. [37] has been developed [26]. In addition, classical information visualization techniques such as parallel coordinates [17] are helpful for the exploration process. Novotny and Hauser [28] propose an optimized parallel coordinates approach based on binning data items that is incorporated also into the visual analysis framework of Akibay and Ma [1]. Such a binning method has been adapted for time series visualizations by Muigg et al. [27].

Besides the fact that very much work is done in nasal airflow simulation as well as in exploratory visual data analysis, to our knowledge, this is the first in-depth visual exploration of nasal airflow phenomena over several simulated breathing cycles under consideration of a comprehensive model of the nasal airways, realistic boundary conditions, and all physically relevant time-varying quantities.

## 2 MODELING AND SIMULATION OF NASAL AIRFLOW

In order to conduct a CFD simulation, the following steps are to be performed:

1. Generation of an adequate geometric model suited for numerical CFD analysis,
2. formulation of a physical model that properly describes fluid flow phenomena, and
3. numerical solution of the associated PDE's.

### 2.1 Anatomical Model of the Upper Respiratory Tract

For this study, a reference model of the nasal airways was created from actual human anatomy without obvious pathological findings. To develop a geometric model, a helical computed tomography (CT) scan of a male volunteer (in fact one of the authors) following local administration of a decongestant was acquired. High-resolution tomography with an almost isotropic spatial resolution of  $0.37 \times 0.37 \times 0.4$  millimeters allows for the representation of internal anatomical structures with sufficient detail (cf. Fig. 2). An individualized geometric model of the

upper respiratory tract was reconstructed from the CT data consisting of trachea, pharynx, nasal and paranasal cavities, the maxillary, frontal and sphenoidal sinuses as well as the ethmoidal cells. Geometric reconstruction of the flow domain was performed using the AMIRA<sup>1</sup> software. Reconstruction comprises multi-material image segmentation, non-manifold boundary surface triangulation, simplification and improvement of surface mesh quality, as well as the generation of a volumetric grid [42]. In view of an airflow simulation the facial skin surface was reconstructed, too (cf. Fig. 3).



Fig. 2. Sagittal, coronal, and axial slices of high-resolution CT data

Special care was taken with the generation of a polygonal mesh of all air-mucosa boundaries as well as the volumetric grid of the enclosed airways, representing a suitable computational domain for a finite element CFD analysis. Different meshes have been generated with the aim of minimizing the element count, the geometric approximation error, and the element distortion. The initial high resolution surface model, consisting of approx. 7.5 million triangles (3.75 million nodes), was simplified and remeshed to approx. 400 000 triangles [42, 44]. The mean simplification error is below  $1/10$  of a millimeter according to the voxel resolution ( $\sigma \approx 0.09 \text{ mm}$ ,  $rms \approx 0.10 \text{ mm}$ ). As a result, a high quality mesh of tissue boundaries has been generated (Fig. 3) with a mean triangular aspect ratio (i.e. the ratio between circumcircle and incircle) of 2.07 within a range of  $[2 \dots 7.5]$  of a possible range of  $[2 \dots \infty)$  (see Table 1).

To ensure accurate numerical calculations for fluid shear stresses, such as changes of air velocity at the mucous walls, dense layers of pentahedral prism elements (2.2 million) have been generated at the air-mucosa and air-skin interfaces (Fig. 3 c, d). From the boundaries of these layers a tetrahedral grid was generated for the enclosed flow domain using an advancing front technique as it is implemented in AMIRA. In addition to the volumetric grid of inner airway structures, a grid of the anterior inflow region was generated to address the effect of the facial morphology on the flow behavior during nasal breathing (cf. Fig. 3 e). Afterwards the grid was optimized with regard to dihedral angles and tetrahedral aspect ratios (ratio between circumsphere and inscribing sphere), resulting in a mean tetrahedral aspect ratio of 4.42 within a range of  $[3 \dots 23.3]$  of a possible range of  $[3 \dots \infty)$ .

Table 1. Properties of the geometric model of the upper respiratory tract.

Properties	Triangulated boundaries	Tetrahedral grid
# of nodes	197 759	325 840
# of cells	396 588 triangles	1 316 100 tetrahedra
Aspect ratio	mean 2.07 ( $\sigma$ 0.10)	mean 4.42 ( $\sigma$ 0.92)
Smallest Angle	mean 51.6 ( $\sigma$ 4.6) $^\circ$	mean 32.2 ( $\sigma$ 23.1) $^\circ$
Largest Angle	mean 69.4 ( $\sigma$ 5.9) $^\circ$	mean 51.9 ( $\sigma$ 16.4) $^\circ$
Edge length	mean 0.12 ( $\sigma$ 0.16) mm	mean 0.09 ( $\sigma$ 0.05) mm
Quality [0,1]	mean 0.97 ( $\sigma$ 0.04)	mean 0.70 ( $\sigma$ 0.12)

The geometrical reconstruction lead to an unstructured, mixed element mesh of the entire computational domain with locally controlled resolution consisting of approx 3.5 million elements (tetrahedra and prisms) with triangular and quadrangular boundary faces. This FE mesh was finally exported in CFD General Notation System (CGNS) format for import into ANSYS CFX<sup>2</sup> software [36].

<sup>1</sup> <http://amira.zib.de>

<sup>2</sup> <http://www.ansys.com/products/cfx.asp>

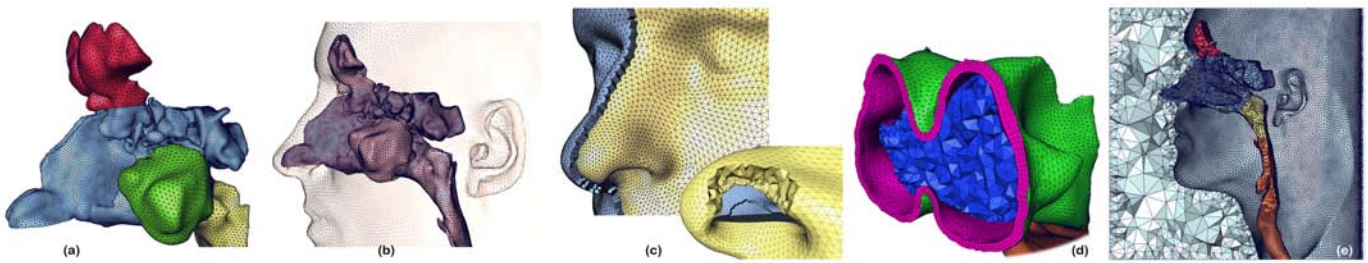


Fig. 3. Geometric model of the flow domain: Remeshed non-manifold tissue boundaries (a, b), unstructured, hybrid (mixed-element) grid (c, d), complete volumetric grid with anterior inflow region (e).

## 2.2 Boundary Conditions of Nasal Breathing

In addition to the CT scan, a series of active anterior rhinomanometry (AARMM) measurements (RhinoLab, HR2) was taken on the same subject in a comparable mucous membrane swelling condition. For a 15 seconds measurement 2000 pressure values were recorded as depicted in Figure 4. These values represent the pressure difference between inlet (nostrils) and outlet (lung) over all breathing cycles.

The relative pressure at the nostrils was assumed as 0.0 Pa – the pressure gradient from the lung side was given with the AARMM measurements acting as boundary conditions for the CFD simulation of nasal breathing. An ambient pressure of 101.325 kPa was chosen. Due to the relatively low speed, air is modeled as an incompressible fluid with a density of  $1.185 \text{ kg/m}^3$  and a dynamic viscosity of  $1.831 \text{ e}^{-5} \text{ kg/(m}\cdot\text{s)}$ . The initial conditions for air temperature and relative humidity were:  $17^\circ \text{ C}$  air temperature in contrast to  $27^\circ \text{ C}$  skin, and  $36.8^\circ \text{ C}$  body temperature, as well as 60% humidity in contrast to 100% on the mucous walls. The nasal mucosa is assumed to be smooth considering flow involved friction.

## 2.3 CFD Simulation of Nasal Breathing

Geometry and boundary conditions are the prerequisites for the CFD simulation of nasal airflow. The fundamental equations of numerical fluid computation are:

- Continuity equation (conservation of mass),
- Navier-Stokes or Reynolds-averaged Navier-Stokes (RaNS) equation (conservation of momentum),
- energy equation (conservation of energy), and
- turbulence equations (in case of RaNS).

These equations define a closed system of coupled non-linear partial differential equations (PDE's) with stochastic character. All conservation equations mentioned above can be written in a generalized form (1) as a transport equation for each mass-related and transported quantity (e.g. velocity  $v$ , enthalpy  $h$ , turbulent kinetic energy  $k$ , rate of turbulent dissipation/vorticity  $\epsilon/\omega$ ), where  $S_\Phi$  is a production term and  $\Gamma_\Phi$  describes the diffusion coefficient of the respective quantity that is to be considered:

$$\frac{\partial}{\partial t}(\rho\Phi) + v_j \frac{\partial}{\partial x_j}(\rho\Phi) = \Gamma_\Phi \frac{\partial^2 \Phi}{\partial x_j^2} + S_\Phi \quad (1)$$

For our simulations, particular attention was paid to turbulence modeling. Therefore, the Shear-Stress-Transport (SST) turbulence model [16] was used. This model combines the  $k/\epsilon$  and the  $k/\omega$  turbulence models [38] with the help of a blending function, which is 1 near the boundaries, i.e. near-wall region, (activating the  $k/\epsilon$  model), and 0 (choosing the  $k/\omega$  model) in the outer part of the flow, as well as for free shear flows. The humidification of nasal airflow was considered as a multi-component flow with an additional transport equation for water vapor. Diffusion and convection were taken into account, both, within the volume and near the mucous walls. Thus, the humidity charge of the nasal mucosa as well as the humidity transfer between mucosa and air could be modeled and simulated.

Based on several steady state calculations, a grid independence study has been conducted, comparing the measured volume flow with computed values for different mesh resolutions. A resolution of about 3.5 million elements and beyond did not produce a significant change of the total flow rate anymore ( $< 1\%$ ). The variation of the pressure difference between inflow and outflow region, and the computation of airflow changes (pressure drop, flow rate) during both inhalation and exhalation allow for a comparison of computed rhinomanometry with the effective readings of the AARMM. For this particular anatomy a slight difference between right and left has been measured, that indeed correlates with our simulation results under the assumption of a non-varying geometry during the respiration cycle (cf. Fig. 4).

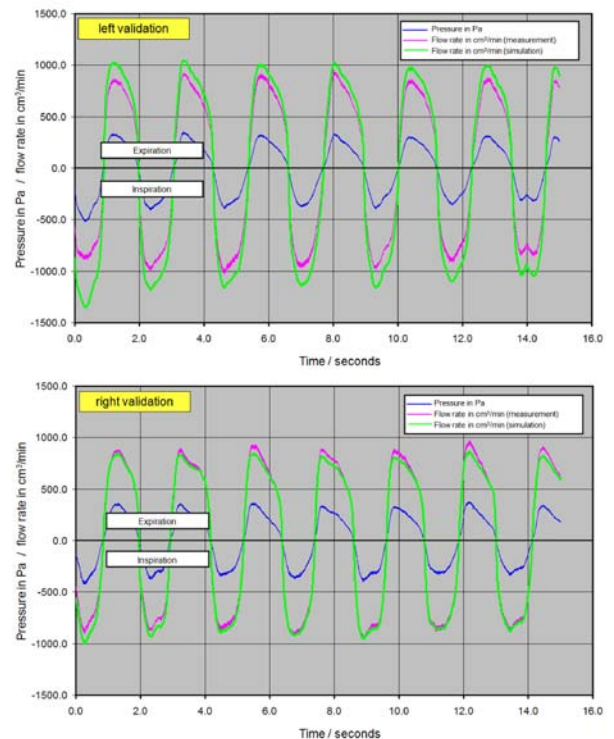


Fig. 4. Validation of simulation results per side: Measured flow rate (pink) vs. simulated flow rate (green), reference pressure in blue.

The final CFD simulation involved calculating the transient flow behavior over the measured breathing cycles under consideration of all given boundary conditions. Iterative methods were used, as they are implemented within ANSYS CFX, to solve the resulting large but sparse, non-linear set of equations (8 iterations per time step of 0.01 s). The computation of one breathing cycle took approx. 72 hours on 8 processors (3.2 GHz). The simulation of several breathing cycles lead to a huge set of flow quantities being exported in 300 time steps with 50 ms intervals (85 GB). This data set is the basis for our investigation of nasal breathing.

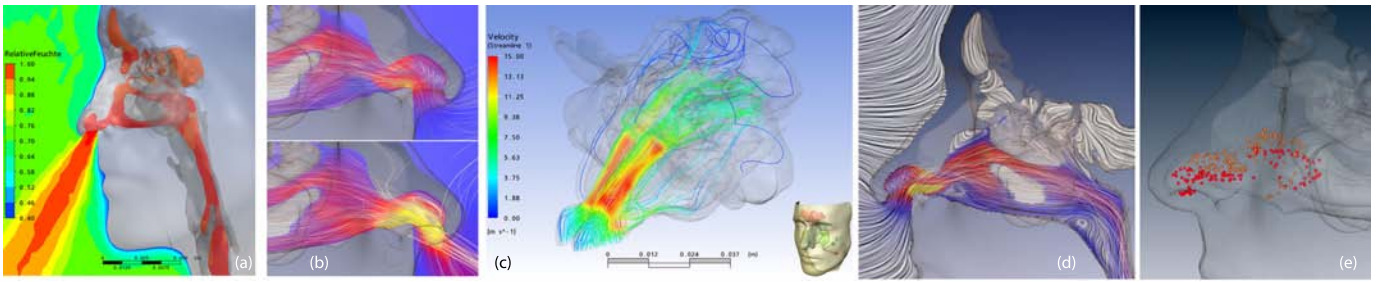


Fig. 5. Visualization of flow quantities: Relative humidity for an exhalation state (a), flow velocity within the nasal cavity (b) during inhalation (top) and exhalation (bottom), inspiratory flow velocity of up to 15 m/s with color coded stream lines (c), illuminated streamlines with color coded planar LIC visualization (d), and particle visualization along field lines with discrimination of left and right side (e).

### 3 VISUAL EXPLORATION OF CFD SIMULATION RESULTS

There are three possibilities to evaluate time-dependent field variables, such as velocity, pressure, temperature, humidity, turbulence quantities, etc.: 1) visualization of individual time steps, 2) visualization of changes between time steps, and 3) visualization of developments within finite time intervals. In this work we focus on the first two techniques. The AMIRA software was used for the visualization of single time steps (stationary flow analysis), and the SimVis<sup>3</sup> software was used for the exploration of flow dynamics (transient flow analysis).

#### 3.1 Stationary Flow Analysis

To obtain an overview of the simulation results, individual time steps of the inhalation and exhalation phases were selected and the respective flow quantities were visualized. Since all data is encoded on volume cells of an unstructured grid, appropriate visualization methods are to be used. For stationary analysis we employed techniques such as color coding of scalar or vector valued quantities, contour plots, iso-surfaces, vector visualization, line integral convolution (LIC), streamline and particle visualization with an animation of seeded streamlines or particles along respective field lines (cf. Fig. 5). These techniques are provided by the AMIRA software [34] that has already been employed for the geometric modeling in this work.

Due to its ease, we made heavy use of the possibility to visualize any quantity on top of arbitrarily oriented planes with an appropriate color coding scheme. In Figure 5 (b), for instance, we see on a section of the nasal cavity that for inhalation (top view) and exhalation (bottom) the main path of airflow differs. Note that the lung induces the flow by creating a reduced pressure, causing air flowing into the nose. Thus, inflow is rather non-directional, whereas outflow is directed due to the shape of the nose. Temperature and humidity are also visualized in this manner (cf. Fig. 5 a), enabling us to assess inhalation and exhalation while obtaining a first impression of the scalar distribution and being able to check the correctness of boundary conditions. Iso-surfaces were generated to locate pressure minima, and LIC techniques were best suited for the understanding of flow structures [4] as shown in Figure 5 (d). A visualization of the flow velocity during inhalation and exhalation using color coded streamlines yields a good overview of spatial flow characteristics for individual time steps. Looking at the velocity field, for example, we can easily grasp the flow structure and see that a maximum of up to 16 m/s is reached within the main nasal cavity (Fig. 5 c). In Figure 5 (b) we used illuminated streamlines in combination with color coded planar cuts, mapping the magnitude of velocity to color values. Even for a single time step the flow field yields enough information to visualize flow characteristics in an animated fashion. Illuminated streamlines can be animated with Amira [35], as well as particles that - after being seeded - move along the streamlines [31] to visualize flow direction (Fig. 5 e). Seeding of streamlines or particles can be accomplished, for instance, by locating pressure minima in order to visualize vorticity.

All these techniques allow for a first visual exploration of the data. The challenge is to locate important flow features and to apply ap-

propriate visualization techniques to emphasize them. The spatio-temporal relations, however, cannot be easily assessed in this manner. Therefore a transient flow analysis is needed.

#### 3.2 Transient Flow Analysis

Without prior knowledge of relevant features in multi-variate, time-dependent 3-D data, the exploration is a highly demanding task that typically necessitates interactive approaches. On the other hand, visual analysis and data exploration often turns out to be difficult or even impossible without employing semi-automatic visualization methods that require only minimal user interaction. Thus, we employed SimVis, a highly interactive visualization system with basic built-in data analysis tools. Furthermore, we extended SimVis to identify features and to obtain findings from which hypotheses regarding physiological processes of nasal breathing can be derived.

##### 3.2.1 Multiple Linked Views for Feature Selection

The framework being used to perform the transient flow analysis provides multiple linked views for concurrent visualization, exploration, and analysis of multi-variate data. Within the scope of our exploration we utilized multiple 3-D views in combination with several types of attribute views, e.g. scatterplots, (see Fig. 8 c), histograms, parallel coordinates [28, 1] (d), or time series visualizations (e, f) in order to obtain an overview of the flow data. The interactive brushing functionality that is provided by all attribute views enables us to select data regions that exhibit interesting behavior. Our feature selection results in multiple *Degree of Interest (DOI)* volumes each storing a scalar field that equals 1 in relevant and 0 in negligible regions of the data set. Since flow data usually are smooth, it is difficult to sharply discriminate between relevant and irrelevant data regions. Thus, unsharp, i.e. non binary DOI values were applied ( $DOI \in [0 \dots 1] \subset \mathbb{R}$ ) to convey this uncertainty. Moreover, such DOI attributions can be combined using fuzzy logic operations in order to derive even more complex features [7].

##### 3.2.2 Volume Rendering Techniques

For an interactive exploration of complex spatio-temporal data via Scientific Visualization (SciVis) methods such as volume rendering, any feature selection within attribute views necessitates an immediate visual feedback on the respective spatial location. In this regard, the nasal airflow data pose two main challenges: First, the underlying unstructured grid is fairly large (1.3 million tetrahedra and 2.2 million prisms which in total roughly equal 8 million tetrahedra), and second the complex anatomical structure of the nasal airways with all of its cavities may lead to occlusion problems and visually cluttered images (cf. Fig. 6, left and right). We tackle these problems by utilizing two different volume rendering techniques. In Fig. 8 (b) a *point-based* overview rendering of the nasal airway data is shown. In this example, volume cells are represented by Gaussian splats that are blended while being rendered in back to front order. Data regions that have not been selected by the user (i.e.,  $DOI = 0$ ) are rendered with low opacity and no color, whereas selected features are displayed less transparently with color that is computed from the data attributes via an appropriate transfer function.

<sup>3</sup> <http://www.simvis.at>

The main advantage of this rendering approach is its performance, as long as the viewing direction remains constant (otherwise an expensive visibility sort becomes necessary). This approach was used to interactively explore the spatio-temporal evolution of selected features and to rapidly switch between different time steps. Main drawbacks of this method are the low rendering quality (circular Gaussian splats only approximate polyhedral cells) as well as the lack of a distinct visualization of object boundaries.

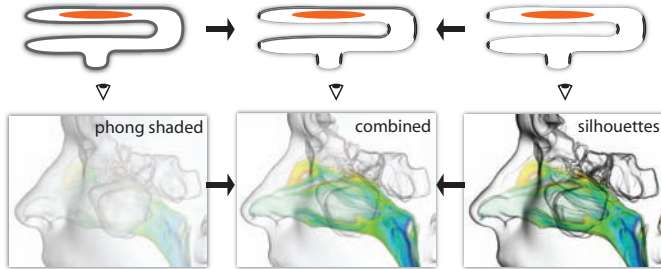


Fig. 6. Comparison of boundary visualization methods.

In contrast to the point-based approach, a volume rendering based on *ray-casting* allows for a visualization of different semi-transparent boundaries. Only regions with  $DOI > 0$  are visualized using volume rendering, whereas unselected portions of the data set are skipped by our ray-casting implementation. Choosing a suitable rendering mode for boundaries is essential as they provide context information that enables us to locate selected features within spatial structures. Fig. 6 (left, right) shows two different boundary surface rendering methods: On the left, a transparent Phong shaded surface rendering is used, whereas on the right a shading model with silhouette enhancement is chosen. Obviously, both approaches are not necessarily adequate for the presented case; the surface rendering lacks contrast because the selected feature within the nasal cavity is occluded by multiple irrelevant surfaces. The silhouette rendering, however, introduces visual clutter, thus making it difficult to grasp spatial relations.

Therefore, we chose a combination of both visualization methods by using surface shading for all object boundaries facing away from the observer, and silhouette enhancement for front facing faces only, as shown in Fig. 6 (center). This rendering technique effectively halves the number of surfaces occluding volumetric features while still supplying enough depth queues by rendering back facing surfaces. In addition, silhouette rendering adds detail for front facing surfaces. For a correct composition of transparent surface and volume rendering an extended depth peeling method is applied [26].

### 3.2.3 Parallel Coordinates

Parallel coordinates are generally suited for exploring relationships between multiple attributes. Their visualizations, however, tend to become increasingly cluttered the more data items (cells of a grid) are to be considered [28]. In order to reduce visual clutter, inherent to parallel coordinates when visualizing millions of data entries, we propose a technique based on the diffusion of a noise texture via a 2D field of  $2 \times 2$  tensors. This tensor field is constructed by computing  $\frac{1}{N} \sum_{i=1}^N \mathbf{v}_i \mathbf{v}_i^T$ , per pixel, with  $N$  being the number of lines covering the image pixel and  $\mathbf{v}_i$  the direction of the  $i^{th}$  line in image space. The resulting tensor per pixel encodes directional information on all lines passing through that particular pixel as illustrated in Fig. 7: On the left the directions of the lines through a pixel are not uniformly distributed around that pixel; this results in an anisotropic tensor visualized by the red ellipse (each ellipse is constructed from the eigenvectors of the respective tensor). Lines with uniformly distributed directions passing through an image pixel result in an isotropic tensor as illustrated on the right hand side of Figure 7. Simple diffusion is performed on a noise texture via the tensor field in order to create a pattern that is blurred along the predominant line direction at each image pixel (see inlays in Fig. 7). We use 16 iterations with a  $7 \times 7$  Gaussian filter kernel to achieve sufficient image quality retaining interactive frame

rates with our current GPU implementation. The main advantage of using this approach is that even when drawing a large number of lines on top of each other (in the example shown in Fig. 8 (d) 21 time steps are visualized resulting in about 75 million lines), the user is still able to recognize trends which otherwise could easily have been missed. Such a scalable implementation of parallel coordinates turned out to be very useful for the visual exploration of the high dimensional attribute space of the nose breathing data set (Fig. 8 d).

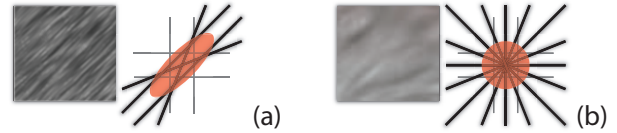


Fig. 7. Different line direction distributions through an image pixel result in anisotropic (a) or isotropic (b) tensor representations that can be used for blurring a noise texture in the parallel coordinate view.

### 3.2.4 Visual Exploration

To gain insight into multi-variate, spatio-temporal data a generic workflow can be followed which closely matches the information seeking mantra: *"Overview first, zoom and filter, then details-on-demand"* as proposed by Shneiderman [33]. At first, the user typically needs to get a general idea of all potentially interesting data attributes and their spatial distribution within the simulated domain. This can be achieved by setting up an exploration session as shown in Fig. 8. As a starting point simple selections (e.g. high or low attribute values) are defined by the user within a particular attribute view, whereas all other linked views are simultaneously updated.

This initial step is illustrated in Fig. 8 where relatively cold air (up to  $23.5^\circ\text{C}$ ) is selected by the lower brushing rectangle (Fig. 8 c) to obtain an overview of the aerodynamic heating during the inhalation phase of the first breathing cycle. An additional selection of warmer air (between  $29^\circ$  and  $31^\circ\text{C}$ ) was defined in order to highlight regions which have already been heated by the mucous walls, but still being colder than the air within the paranasal cavities. Both selections do represent a feature that can be explored in all other views shown in Fig. 8. The 3-D visualization in Fig. 8 (a) displays these features 450 ms after the first breathing cycle has started. The two parts of the selected data region (cold and heated air) can be differentiated by their coloring, where blue-green corresponds to colder flow and red represents the warm air. It can be observed that the main portion of cold air travels along one distinct path as indicated by the dotted line and is heated approximately  $4.5^\circ\text{C}$  during its traversal. Note that a reservoir of warm air is located below the dotted line as indicated by the label. Further exploration of this feature will be conducted in subsequent sections.

A second notable structure can be seen on the left hand side of Fig: 8 (a) behind the nasal valve: The geometry of the nasal isthmi (the narrowest passage between nostrils and nasal atrium) appears to result in vortical flow which again leads to early mixing of warm and cold air, as indicated by the black arrow. The overview visualization presented in Fig. 8 (b) illustrates the same features as in (a), but with flow velocity mapped to color. Focusing on high velocity regions of the selected data, the main trajectory of the inhaled air can be discerned. Note that in the region of the olfactory epithelium the airflow velocity during the inhalation phase remains relatively low, resulting in a preservation of humidity and warmth which again are optimal conditions for the reaction between scent molecules and sensory receptors. Furthermore, the relatively high air velocity in the middle passage of the nasal cavity suggests that due to the resulting pressure drop within the inhalation phase a ventilation of the frontal and maxillary sinuses occurs which are connected to the nasal cavity via small ducts.

The temporal development of the selected features has not yet been investigated in detail. Even though the scatterplot that was used to select the cold and warm air is capable of displaying a selected time-interval, the overall evolution of features over time is difficult to comprehend. Thus, a time series visualization similar to approaches proposed by Akibay and May [1] and Muigg et al. [27] has been used to

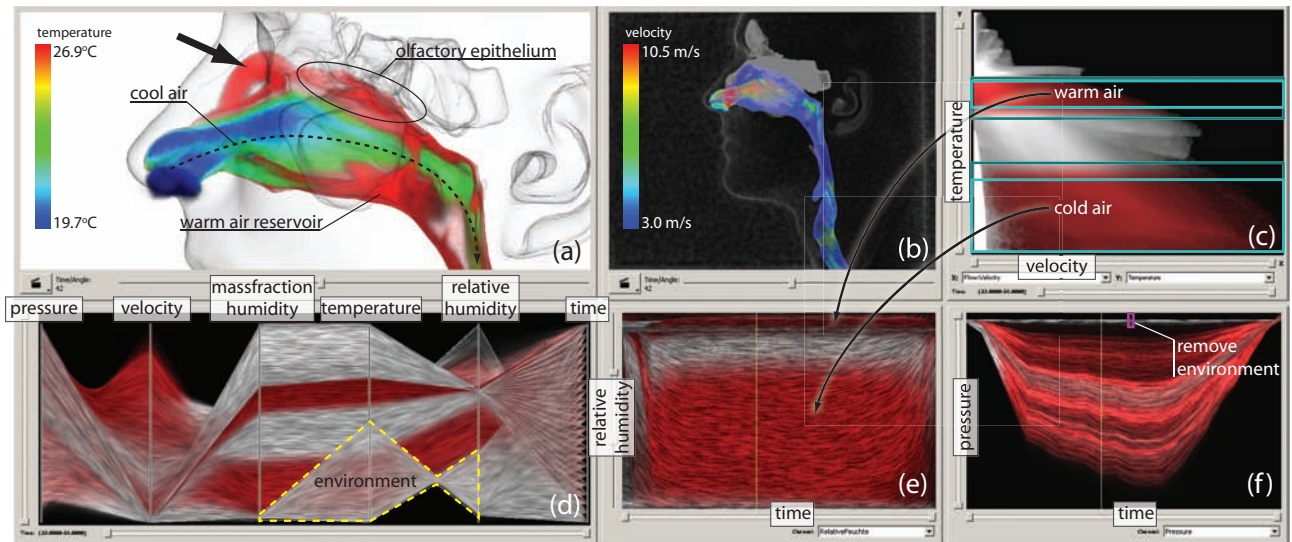


Fig. 8. Overview of a visual exploration session: Different attribute views (c), (d), (e), and (f) are used to interactively select data regions of interest which can be examined and modified in all other visualizations. The 3-D views (a) and (b) display the selections within their spatial context.

plot the selected feature over time within the context of an additional data attribute (cf. Fig. 8). Here, for each volume cell the actual relative humidity (e) and the pressure (f) are plotted over time (x-axis). Color indicates to which degree a curve is selected (red equals fully selected and white represents unselected data) whereas brightness represents the number of curves overlapping each other. The vertical yellow line indicates the current time step and is linked to both time series views in correspondence to the 3-D visualizations where the respective state of the selected data is displayed.

Since the SimVis framework does not yet support the selection of semantically different portions of a flow domain (e.g., environment or nasal airways) the time series view for the pressure attribute (Fig. 8 f) was used to exclude the anterior inflow region from all selections by employing an inverted *time step brush* that is represented by the pink rectangle. This brush defines a *DOI* function which is 0 if the associated scalar attribute at a particular time step lies within a user defined interval (in this case a relative pressure close to 0 Pa) - and 1 otherwise. As a reference, the time step of maximal negative pressure at the interface to the lung was selected since it exhibits the strongest pressure gradient between the nasal airways and the environment.

The humidification of inhaled air is another important physiological function of the nasal airways. Fig. 8 (e) gives an overview of the temporal development of the relative humidity within the upper respiratory tract. By investigating its progression, which is indicated by a visualization approach based on line integral convolution, a steep drop in relative humidity can be observed which stabilizes after approximately 200 ms. Note that the warm/cold air feature previously defined in the scatterplot is shown as two distinct red regions in the respective visualization. The region of higher humidity corresponds to the warm air selection whereas the drier air corresponds to the selected region with lower temperature. After 700 ms the relative humidity increases again since low pressure from the lung diminishes (see Fig. 8 f).

The pressure-time curves shown in Fig. 8 (f) enable us to relate time steps of interest to the entire breathing cycle. Looking at the visualization it becomes apparent that after a short period of time (roughly 150 ms) the basic distribution of pressure values remains constant with respect to scaling (i.e., there are no curves crossing each other). This means that after an initial turbulent phase between exhalation and inhalation, flow features, such as vortices, remain fairly stationary.

In Fig. 8 (d) our parallel coordinates implementation is used to gain an overview of the selected data regions in multiple additional data dimensions. Like in all other attribute views currently selected features are highlighted in red whereas the remaining data is shown in white/grey. The axes correspond to the scalar attributes pressure, velocity, mass fraction of humidity, temperature, relative humidity, and

time. At a first glance, a strong correlation between mass fraction of humidity and temperature can be recognized (this assumption is further confirmed by the horizontally blurred noise indicating that most of the lines are parallel to the x-axis). In addition, at least the selected data regions exhibit a correlation between temperature and relative humidity. Furthermore, a negative correlation between flow velocity and mass fraction humidity can be observed. As with the scatterplot we also explored the temporal distribution of the data values by interactively selecting time intervals for visualization. The region of the data set outlined in yellow and marked with "environment" in Fig. 8 (d) corresponds to the anterior inflow region that, as mentioned earlier, was excluded from the selections via a time step brush (Fig. 8 f).

### 3.2.5 In-Depth Visual Analysis

After an initial exploration of the nasal airflow data, the next step of our investigation corresponds to the "*zoom and filter*" portion of Shneiderman's mantra. In order to gain more insight into nasal breathing we use our analysis framework to derive additional information such as spatial/temporal gradients or even more complex flow parameters such as  $\lambda_2$  [19]. This information can then be used to further restrict/modify previously defined features, thus enabling us to hypothesize about phenomena being observed in the course of our exploration.

Below we present an in-depth analysis of two distinct features: Fig. 9 shows an overview of three different time steps: 100 ms, 600 ms, and 1 s after the beginning of the inhalation phase which lasts roughly 1.05 s. On the very right of Fig. 9 an additional inferior view is shown 600 ms after the beginning of the inhalation phase. In the middle row a selection is depicted which is based on the warm air feature that was explained in the previous section. This selection has been further restricted to low velocity regions and temperature is mapped to color. The accompanying inlets show the parallel coordinates views at corresponding time steps that were used to define the selection via two brushing rectangles (indicated in yellow). In the top row of images the warm/slow air feature was further restricted to vortical regions within the flow, as defined by  $\lambda_2$ . Color is mapped to the strength of vorticity indicating weak (green) and strong (red) vortical air motion. The inlets shown in the top row provide an overview of all vortical regions without any restriction to warm/slow flow regions.

The first finding discussed in this section is the early mixing of cold and warm air behind the nasal valve. It is notable that this process is much stronger on the left side of the nose than on the right. This can be seen clearly at 600 ms when comparing the selected regions indicated by (L) and (R). The difference is caused by a slight asymmetry in the nasal anatomy as shown in the close-up image. Here, two different (weak) vortices, which are indicated as grey dotted lines, originate

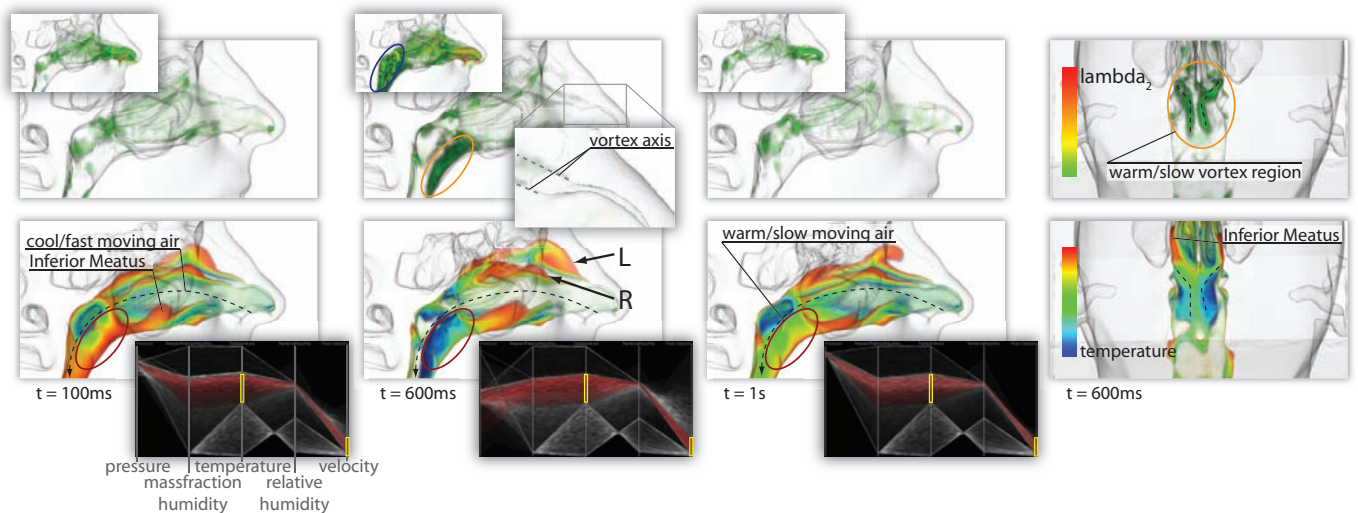


Fig. 9. Different time steps of a feature defined by low flow velocity and relatively high temperature in the middle row. In the top row the feature is further restricted to vortical regions as defined by the  $\lambda_2$  criterion. On the very right an additional inferior view illustrates how vortex regions can be related to heat distribution. The parallel coordinate plots show the data at corresponding time steps.

behind the nasal isthmi. On the left side of the nose the progression of the vortex points slightly up which results in a stronger expression of this feature. This demonstrates how minor deviations in the nasal geometry may already have a major effect on the airflow, which has to be taken into account for therapy planning in rhinosurgery.

Another finding that has already been hinted at in the previous overview is related to the existence of a warm air reservoir in the nasopharynx, visible in all three time steps in Fig. 9 (see red ellipses). This is remarkable since all inhaled air must pass through this region and it was assumed that its relatively high speed does not promote any warming. However, all selected regions shown in the middle row of Fig. 9 do represent warm but slow moving air (as selected in the parallel coordinates view). This indicates that most of the fast moving cold air is traveling along the trajectory already identified in Fig. 8 (a). A main cause for this seems to be a complex system of vortices located in the upper regions of the nasopharynx marked by the blue ellipse in the close-up picture on top at 600 ms. It shows vortical regions without the restriction to warm/slow air with color indicating vortex strength. Below the vortex system, that is transporting fast/cold air, the aforementioned slowly moving air is warmed up. This process is further supported by a secondary system of two parallel vortices indicated by the ellipses colored in orange (Fig. 9). The vortices originate at the transition between nasopharynx and the inferior meatus on both sides of the nasal airways (axes indicated as stippled lines). Note how they constitute the shape of the regions of slow moving warm air.

#### 4 CONCLUSIONS & FUTURE WORK

A visual exploration of nasal airflow for several simulated breathing cycles has been presented. Fluid flow simulations are based on a comprehensive geometric model of the upper respiratory tract as well as realistic boundary conditions under consideration of physically relevant quantities such as pressure, temperature, and humidity. CFD simulations of several breathing cycles lead to 85 GB of time-dependent multi-variate flow data that have been visually analyzed within this work. Both, anatomy reconstruction and visual exploration of the data required combinations of advanced interactive, semi-automatic and automatic modeling, visualization, and data analysis techniques.

For a stationary analysis of the simulation data we employed techniques for scalar and vector field visualization, such as color coding, contour plots, iso-surfaces, line integral convolution, streamline visualization, and tracing of seeded particles. This already led to interesting observations such as major differences between the progression of inhaled and exhaled air within the nasal cavities.

In order to gain an overview of the temporal characteristics of the flow data we used multiple linked views for concurrent visualization, exploration, and analysis – employing 3-D views in combination with several types of attribute and time series visualizations. Specific challenges imposed by data size and geometric complexity have been addressed by utilizing different volume rendering implementations as well as a scalable parallel coordinates implementation. Interactive brushing and linking techniques enabled us to define and investigate data regions that exhibit interesting behavior such as vortex systems in the lower part of the nasopharynx which might be related to warming inhaled air, or early mixing of inhaled air with warm air in the nasal valve region. A visual exploration framework enables researchers to understand how their data fits into the context of known conceptions or beliefs and accelerates the process of generating testable hypotheses.

- The differing courses of airflow in inspiration and expiration due to the nasal geometry suggest an airway resistance that not only depends on the nasal valve but also varies with flow direction.
- The more cranial course of the inhaled air supports an adequate presentation of odor molecules to the olfactory receptors. During exhalation, the direction of warm and humid air to the olfactory epithelium possibly creates optimal climate conditions for the smelling process, while providing a retrograde transport of odor molecules from the oropharynx to the olfactory slit.
- The nasal isthmus obviously has a strong impact on the distribution of the air stream. Its geometry not only seems to be significantly responsible for the nasal airflow resistance but also relevant for directing air during the inhalation phase.
- The air stream through the middle meatus within the initial inspiration phase has a particularly high velocity. Consequently, the resulting static pressure differences at the sinus ostium may provide an appropriate ventilation of the sinuses.
- The omnidirectional inspirational flow in contrast to the directed expirational flow refutes the widely held belief that a hanging tip automatically induces nasal obstruction.

Finally, it should be noted that the analysis of the flow data was quite laborious due to the lack of initial hypotheses, thus requiring a visual exploration of *all* attributes. Future work might involve research on methods comparable to VisTrails [3]. Furthermore, the unfamiliar multi-view setup initially posed challenges to our domain experts. Still after a training period, the ability to interactively define different queries while immediately being able to assess results was highly appreciated and significantly improved the investigation.

In our future work we shall address the extraction of Lagrangian features and coherent structures. This might allow us to confirm our current findings and investigate further details, as for example the difference between regular and irregular flow.

## ACKNOWLEDGMENTS

The authors thank Dr. Alexander Steinmann, CFX Berlin Software GmbH, Prof. Dr. Werner Heppt, ENT department of the Clinical Center Karlsruhe, Germany, as well as Steffen Hadlak, University of Rostock. Parts of this work were funded by the Austrian Research Funding Agency (FFG) in the scope of the projects "AutARG" (No. 819352) and "PolyMulVis" (No. 815377).

## REFERENCES

- [1] H. Akiba and K.-L. Ma. A tri-space visualization interface for analyzing time-varying multivariate volume data. In *Proc. of EuroVis07*, pages 115–122, 2007.
- [2] N. Bailie, H. Brendan, J. Watterson, and G. Gallagher. An overview of numerical modeling of nasal airflow. *Rhinology*, 44:53–57, 2006.
- [3] L. Bavoil, S. P. Callahan, C. E. Scheidegger, H. T. Vo, P. Crossno, C. T. Silva, and J. Freire. Vistrails: Enabling interactive multiple-view visualizations. In *Proc. of IEEE Visualization*, pages 745–747. IEEE Computer Society, 2005.
- [4] B. Cabral and L. C. Leedom. Imaging vector fields using line integral convolution. In *Proceedings of SIGGRAPH 93*, pages 263–272, 1993.
- [5] H. Doleisch. SIMVIS: interactive visual analysis of large and time-dependent 3D simulation data. In *Proc. of Winter Simulation Conference*, pages 712–720, 2007.
- [6] H. Doleisch, M. Gasser, and H. Hauser. Interactive feature specification for focus+context visualization of complex simulation data. In *VISSYM '03*, pages 239–248, 2003.
- [7] H. Doleisch and H. Hauser. Smooth brushing for focus+context visualization of simulation data in 3D. In *Proc. of WSCG 2002*, pages 147–154, 2002.
- [8] H. Doleisch, M. Mayer, M. Gasser, P. Priesching, and H. Hauser. Interactive feature specification for simulation data on time-varying grids. In *Proc. of SimVis 2005*, pages 291–304, 2005.
- [9] H. Doleisch, P. Muigg, and H. Hauser. Interactive visual analysis of hurricane Isabel with SimVis. Technical Report TR-VRVis-2004-058, VRVis Research Center, Vienna Austria, 2004.
- [10] D. Doorly, D. J. Taylor, P. Franke, and R. C. Schroter. Experimental investigation of nasal airflow. *Proc. IMechE 2008, Part H, J. Engineering in Medicine*, 222:439–453, 2008.
- [11] D. J. Doorly, D. J. Taylor, A. M. Gambaruto, R. C. Schroter, and N. Tolley. Nasal architecture: form and flow. *Phil. Trans. R. Soc. A*, 366:3225–3246, 2008.
- [12] G. P. Galdi, R. Rannacher, A. M. Robertson, and S. Turek. *Hemodynamical Flows: Modeling, Analysis and Simulation (Oberwolfach Seminars)*. Birkhuser, 1. edition, 2007.
- [13] G. J. M. Garcia, N. Bailie, D. A. Martins, and J. S. Kimbell. Atrophic rhinitis: a CFD study of air conditioning in the nasal cavity. *J Appl Physiol*, 103:1082–1092, 2007.
- [14] M. P. Garrity. Raytracing irregular volume data. *ACM Computer Graphics*, 24(5):35–40, 1990.
- [15] D. L. Gresh, B. E. Rogowitz, R. L. Winslow, D. F. Scollan, and C. K. Yung. Weave: a system for visually linking 3-D and statistical visualizations, applied to cardiac simulation and measurement data. In *Proc. of IEEE Visualization '00*, pages 489–492, 2000.
- [16] H. Grotjans and F. R. Menter. *Wall functions for industrial applications*, pages 1112–1117. John Wiley & Sons, 1998.
- [17] A. Inselberg and B. Dimsdale. Parallel coordinates: a tool for visualizing multidimensional geometry. In *Proc. of IEEE Visualization '90*, pages 361–378. IEEE Computer Society, 1990.
- [18] S. Ishikawa, T. Nakayama, M. Watanabe, and T. Matsuzawa. Visualization of flow resistance in physiological nasal respiration - analysis of velocity and vorticities using numerical simulation. *Arch Otolaryngol Head Neck Surg*, 132:1203–1209, 2006.
- [19] J. Jeong and F. Hussain. On the identification of a vortex. *Journal of Fluid Mechanics Digital Archive*, 285(-1):69–94, 1995.
- [20] J. Kehler, F. Ladstädter, P. Muigg, H. Doleisch, A. Steiner, and H. Hauser. Hypothesis generation in climate research with interactive visual data exploration. *IEEE TVCG*, 14(6):1579–1586, 2008.
- [21] V. Kulish and M. Kanoh. *Human Respiration: Anatomy And Physiology, Mathematical Modeling, Numerical Simulation And Applications (Advances in Bioengineering, No 3)*. WIT Press, 2006.
- [22] R. S. Laramee, H. Hauser, H. Doleisch, F. H. Post, B. Vrolijk, and D. Weiskopf. The state of the art in flow visualization: Dense and texture-based techniques. *Computer Graphics Forum*, 23(2):203–221, 2004.
- [23] J. Lindemann, H.-J. Brambs, T. Keck, K. Wiesmiller, G. Rettinger, and D. Pless. Numerical simulation of intranasal airflow after radical sinus surgery. *American Journal of Otolaryngology Head and Neck Medicine and Surgery*, 26:175–180, 2005.
- [24] J. Lindemann, T. Keck, K. Wiesmiller, B. Sander, H.-J. Brambs, G. Rettinger, and D. Pless. Nasal air temperature and airflow during respiration in numerical simulation based on multislice computed tomography scan. *Am J Rhinol*, 20:219–223, 2006.
- [25] G. Mlynski. *Physiology and Pathophysiology of Nasal Breathing*, pages 75–87. Thieme, 2004.
- [26] P. Muigg, M. Hadwiger, H. Doleisch, and H. Hauser. Scalable hybrid unstructured and structured grid raycasting. *IEEE TVCG*, 13(6):1592–1599, 2007.
- [27] P. Muigg, J. Kehler, S. Oeltze, H. Piringner, H. Doleisch, B. Preim, and H. Hauser. A four-level focus+context approach to interactive visual analysis of temporal features in large scientific data. *Computer Graphics Forum*, 27(3):775–782, 2008.
- [28] M. Novotny and H. Hauser. Outlier-preserving focus+context visualization in parallel coordinates. *IEEE TVCG*, 12(5):893–900, 2006.
- [29] D. Pless, T. Keck, K. Wiesmiller, G. Rettinger, A. J. Aschoff, T. R. Fleiter, and J. Lindemann. Numerical simulation of air temperature and airflow patterns in the human nose during expiration. *Clin. Otolaryngol.*, 29:642–647, 2004.
- [30] F. H. Post, B. Vrolijk, H. Hauser, R. S. Laramee, and H. Doleisch. The state of the art in flow visualization: Feature extraction and tracking. In *Computer Graphics Forum*, volume 22(4), pages 775–792. 2003.
- [31] I. A. Sadarjoen, T. van Walsum, A. J. S. Hin, and F. H. Post. Particle tracing algorithms for 3D curvilinear grids. In *Scientific Visualization: Overviews, Methodologies, and Techniques*, pages 311–335. IEEE Computer Society, 1997.
- [32] T. Shakked, D. Katoshevski, D. M. Broday, and I. Amirav. Administration of aerosolized drugs to infants by a hood. *Journ. of Aerosol Medicine*, 19(4):533–542, 2006.
- [33] B. Shneiderman. The eyes have it: A task by data type taxonomy for information visualizations. In *Proc. of IEEE VL*, pages 336–343, 1996.
- [34] D. Stalling, M. Westerhoff, and H.-C. Hege. Amira: A highly interactive system for visual data analysis. In C. D. Hansen and C. R. Johnson, editors, *The Visualization Handbook*, pages 749–767. Elsevier, 2005.
- [35] D. Stalling, M. Zöckler, and H.-C. Hege. Fast display of illuminated field lines. *IEEE TVCG*, 3(2):118–128, 1997.
- [36] A. Steinmann, P. Bartsch, S. Zachow, and T. Hildebrandt. Breathing easily: Simulation of airflow in human noses can become a useful rhinosurgery planning tool. *ANSYS Advantage*, 2(1):30–31, 2008.
- [37] M. Weiler, M. Kraus, M. Merz, and T. Ertl. Hardware-based ray casting for tetrahedral meshes. In *Proc. of IEEE Visualization 2003*, pages 333–340, 2003.
- [38] D. C. Wilcox. *Turbulence Modelling for CFD*. DCW Industries, Inc., La Canada, CA, USA, 2nd edition, 1998.
- [39] S. Yu, Y. Liu, X. Sun, and S. Li. Influence of nasal structure on the distribution of airflow in nasal cavity. *Rhinology*, 46:137–143, 2008.
- [40] S. Zachow, A. Steinmann, T. Hildebrandt, and W. Heppt. Understanding nasal airflow via CFD simulation and visualization. In *Proc. Comp Aid Surg Around the Head*, pages 173–176. Pro Business Verlag, 2007.
- [41] S. Zachow, A. Steinmann, T. Hildebrandt, R. Weber, and W. Heppt. CFD simulation of nasal airflow: treatment planning for functional rhinosurgery. In *Computer Assisted Radiology and Surgery*, pages 165–167, Osaka, Japan, 2006. Elsevier.
- [42] S. Zachow, M. Zilske, and H.-C. Hege. 3D reconstruction of individual anatomy from medical image data: Segmentation and geometry processing. In *25. ANSYS Conference & CADFEM Users' Meeting*, Dresden, 2007, and Techn. Report: ZR 07-41, Zuse Institute Berlin, 2007.
- [43] K. Zhao, P. Dalton, G. C. Yang, and P. W. Scherer. Numerical modeling of turbulent and laminar airflow and odorant transport during sniffing in the human and rat nose. *Chem. Senses*, 31:107–118, 2006.
- [44] M. Zilske, H. Lamecker, and S. Zachow. Adaptive remeshing of non-manifold surfaces. *Computer Graphics Forum*, 27(2):211–214, 2008.